Soft Matter

Accepted Manuscript

This is an *Accepted Manuscript*, which has been through the Royal Society of Chemistry peer review process and has been accepted for publication.

Accepted Manuscripts are published online shortly after acceptance, before technical editing, formatting and proof reading. Using this free service, authors can make their results available to the community, in citable form, before we publish the edited article. We will replace this *Accepted Manuscript* with the edited and formatted *Advance Article* as soon as it is available.

You can find more information about *Accepted Manuscripts* in the Information for Authors.

Please note that technical editing may introduce minor changes to the text and/or graphics, which may alter content. The journal's standard Terms & Conditions and the Ethical guidelines still apply. In no event shall the Royal Society of Chemistry be held responsible for any errors or omissions in this *Accepted Manuscript* or any consequences arising from the use of any information it contains.

ROYAL SOCIETY OF CHEMISTRY

www.rsc.org/softmatter

As a RBC passes through a slit, large dissociation stress may develop between its lipid bilayer and the cytoskeleton.

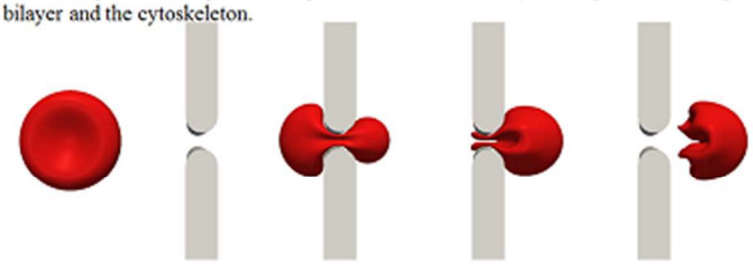

ARTICLE TYPE www. rsc.org/xxxxxx | XXXXXXXX

Deformation and Internal Stress in a Red Blood Cell as It Is Driven Through a Slit by an Incoming Flow

Sara Salehyar and Qiang Zhu*

Received Xth XXXXXXXXXX 20XX, Accepted Xth XXXXXXXXX 20XX
First published on the web Xth XXXXXXXXXX 200X
DOI: 10.1039/b000000x

To understand the deformation and internal stress of a red blood cell when it is pushed through a slit by an incoming flow, we conduct a numerical investigation by combining a fluid-cell interaction model based on boundary-integral equations with a multiscale structural model of the cell membrane that takes into account the detailed molecular architecture of this biological system. Our results confirm the existence of cell 'infolding', during which part of the membrane is inwardly bent to form a concave region. The time histories and distributions of the area deformation, the shear deformation, and the contact pressure during and after the translocation are examined. Most interestingly, it is found that in the recovery phase after the translocation significant dissociation pressure may develop between the cytoskeleton and the lipid bilayer. The magnitude of this pressure is closely related to the locations of the dimple elements during the transit. Large dissociation pressure in certain cases suggests the possibility of mechanically induced structural remodeling and structural damage such as vesiculation. With quantitative knowledge about the stability of intra-protein, inter-protein and protein-to-lipid linkages under dynamic loads, it will be possible to achieve numerical prediction of these processes.

1 Introduction

Due to its simplicity and existing knowledge about its detailed molecular architecture, red blood cells (RBCs) provide an ideal model system for studying the structure versus function of living cells. A mature RBC has no nucleus - it basically contains cytosol enclosed within a highly deformable composite membrane. Conventionally, this membrane is viewed as a two-layer structure. The outer layer refers to the lipid bilayer, which behaves like fluid. The inner layer, the cytoskeleton, is a protein network with 33,000 repeating units called junctional complexes (JCs). A JC is characterized by a 'spoked' structure with a central piece of short actin protofilament surrounded by up to 6 spectrin (Sp) dimers. The neighboring JCs are linked through head-to-head association of these Sp dimers. The cytoskeleton is connected to the lipid bilayer at isolated pinning sites, including the suspension complex (SC) (consisting of band 3, ankyrin, and protein 4.2) and the secondary site (consisting of protein 4.1 and glycophorin C). Hereby band 3 and glycophorin C are transmembrane proteins that penetrate the lipid bilayer. Since the lipid bilayer is fluidic, these transmembrane proteins can drift within it so that the two layers can slide against each other, allowing them to have different local in-plane (area and shear) deformations. The overall surface area of the cell, on the other hand, does not vary much due to the large area stiffness of the lipid bilayer.

Dept. Struc. Engr.,UC San Diego, La Jolla, USA. Fax: 858-822-2260; Tel: 858-822-2161; E-mail: qizhu@ucsd.edu

The RBC membrane exists in a state of dynamic equilibrium as a result of the dynamic balances between associated and dissociated states of many intra-protein, inter-protein, and protein-to-lipid linkages in it. These balances can be disturbed by mechanical loads. According to previous investigations, the connections that may rupture under mechanical loads include: (1) the folded domains inside Sp[1,2], (2) the head-to-head association between Sp dimers that links the neighboring JCs[3,4], (3) the band 3-ankyrin 'bridge' that is the connection between the SC and the lipid bilayer[5], (4) the protein 4.1-band 3 connection[6], and (5) the band 3-lipid bilayer connection[7]. The occurrence of these dissociations will dramatically change the mechanical properties of the membrane, causing structural instability, and even permanently damage the cell (manifested in hemolysis, the bursting of the cell and the release of hemoglobin into the plasma). For example, the rupture of the band 3-ankyrin linkage or the band 3-lipid linkage will cause detachment of the skeleton from the lipid bilayer, leading to vesiculation (or vesicle formation). Vesiculation is associated with membrane loss and dramatic changes in the shape and physiology of the cell. Large in-plane stress in the cytoskeleton (i.e. the stress within the plane of the skeleton itself) may trigger dissociation of the Sp-to-Sp bonds between JCs, leading to changes in the mechanical properties of the cell or even phase transition from elasticity to plasticity[8]. In addition, despite the large area stiffness of the lipid bilayer, sufficiently large mechanical loads may cause unrecoverable expansion of pores on the membrane and eventually cell burst-

ing. According to experiments under quasi-static conditions, the maximum areal strain the membrane can withstand is 2-4%, beyond which it will break[9,10]. Under dynamic loading, the experiments conduced by Li *et al.* through an impulsive stretching experiment suggest that the RBC membrane may be capable of sustaining area expansion as large as 40% without bursting[11].

During circulation, RBCs travel in fluidic channels within endothelial walls. In natural conditions, the cell sustains large dynamic deformations owing to the combined effect of fluid loading and confinements such as capillaries and venous sinuses in the spleen. These loadings may affect the structural integrity of the cell, leading to structural remodeling, phase transition, structural failure and cell dysfunction. The possibility of flow-induced cell damage is more pronounced within artificially-created flow fields inside mechanical circulatory support apparatus (for example artificial blood pumps)[12]. The molecular-level structural stability of a RBC under large dynamic loading is thus essential to its normal function. However, to date there is little knowledge about whether or how these flow-induced structural remodeling and structural failure happen *in vivo*.

One of the most severe environments in circulation occurs inside a spleen, where blood runs from the red-pulp cords (ends of small arterioles) to the venous sinuses and collects back into the venous system. The venous sinuses are made of parallel series of endothelial cells with slits between them. Normal red blood cells can pass through these slits while aged, defected, or infected red blood cells may be stuck there, where they are phagocytosed by macrophages. While most of the existing fluid-cell interaction models concentrate on the dynamics of RBCs in simple shear flows[13–21], inside a tube[22–24], or near a wall[25], there do exist studies about the translocation of RBCs through a slit. For example, *via* systematic simulations Freund has investigated the critical conditions for the cell to successively pass through a slit at different combinations of incoming flow speed, viscosity ratio, cell orientation, and relative position between the cell and the slit[26]. This study has illustrated an interesting cell deformation mode called 'infolding'. When it happens large curvature on the cell membrane is observed, suggesting that large internal strain and stress are indeed possible in this process. A similar setup was examined in an earlier study by Halpern and Secomb[27] using the lubrication theory. In terms of the large cell deformation due to boundary confinement, this scenario is also similar to the passage of RBC through a cylindrical capillary[28,29]. However, in these models the cell membrane is depicted as a single layer of material with uniform properties. No detailed local membrane deformation and internal stress (especially the interaction stress between the cytoskeleton and the lipid bilayer) are examined. In another report the dynamics of a RBC as it passes through a microfluidic channel (with dimensions as small as $2.7\mu\text{m}\times3\mu\text{m}$) was investigated with both experiments and numerical modeling by using a dissipative particle dynamics (DPD) model[30]. The focus was on cell deformation and the effects of various conditions (e.g. size of the channel). The internal stress in the cell was not examined.

The purpose of this study is to numerically investigate the process of a RBC passing through a slit (mimicking the venous system inside a spleen) driven by incoming flow through a multiscale fluid-structure interaction model that accounts for the double-layer structure of the membrane, the molecular-level architecture, and the viscoelasticity of the system. Unlike the aforementioned work, the focus of this study will be on local deformations of the membrane and the skeleton-bilayer contact pressure during the process.

The rest of the paper is organized as follows. We first define the physical problem, including the geometry of the solid boundaries that form the slit as well as the initial orientation of the cell and its initial location with respect to the slit. This is followed by a brief description of the multiscale model of the cell membrane and the boundary-element model of fluid effects (details of these models have been published earlier). Numerical results, including overall cell deformations, detailed in-plane deformations of the membrane, and contact pressure between the cytoskeleton and the lipid bilayer are then discussed. Finally, conclusions are drawn.

2 Physical problem

As shown in Fig. 1, we consider the process of a red blood cell being driven through a slit of width δ by an incoming flow with average speed $\overline{U}$. The slit is formed between two solid boundaries, each of them with width L, height H, and thickness D. The upper and lower ends of these boundaries are rounded with radius $D/2$. The reported ranges for D and δ in human spleen are 0.9-3.2 μm and 0.25-1.2 μm, respectively[31]. In our study we choose $D = 2$ μm and $\delta = 1$ μm. We further set L to be 15 μm and H to be 8.5 μm. Following Freund[26], we render the problem to be triply periodic with periods of 100 μm, 19 μm, and 15.2 μm in x, y, and z directions, respectively.

At its starting position, the horizontal distance from the center of the cell to the slit is 10 μm. The initial orientation of the cell is depicted by two angles, the roll angle θ_0 and the pitch angle ϕ_0. Although the lateral offset between the initial location of the cell and the slit (i.e. the initial distance between the center of the cell to the slit in the y direction) also plays a role in determining the dynamics during the process (e.g. the occurrence of infolding)[26], for simplicity in the present study this parameter is not considered so that we concentrate on the scenario when the center of the cell is initially aligned with the center of slit in both y and z directions.

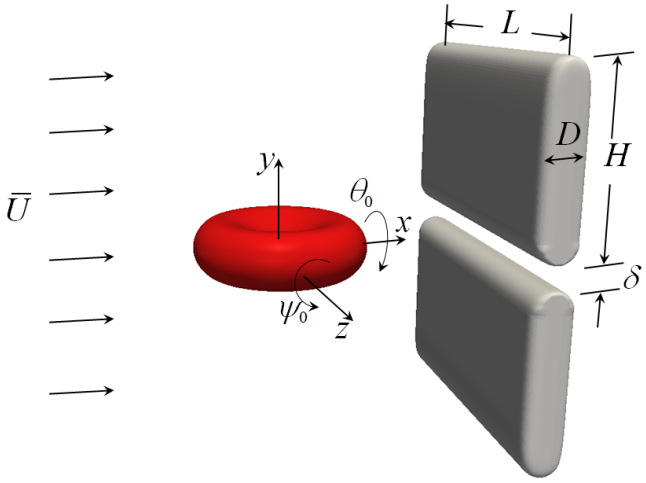

Fig. 1 Definition of the physical problem.

3 Fluid-structure interaction model

We solve the aforementioned fluid-structure interaction problem by combining a boundary-element fluid model with a multiscale structural model of the cell membrane. To elaborate, the fluid model we use is based on the low-Reynolds number assumption and mathematically depicted by boundary-integral equations. In this approach the cell membrane is represented by distributions of Stokeslets, which is then solved using the boundary-element method. In the structural side, the cell membrane is represented by a three-level multiscale model that relates the mechanics of the complete cell to its detailed molecular architecture. In the following we briefly summarize the key components of these models. The details can be found in our previous publications [2,32–34].

3.1 The multiscale structural model

In its current version, our multiscale approach consists of models in three length scales: a complete cell model, a local model that accounts for the junctional complex structure of the protein network, and a molecular-based constitutive model of the Sp (the protein that determines the stiffness of the membrane). In the following key characteristics of these three models are summarized.

In the complete cell model (also referred to as the Level III model), the membrane is represented as two layers of continuum shells [34]. Due to the mobility of transmembrane proteins such as band 3 or glycophorin C inside the lipid bilayer, these two layers are allowed to slide against each other so that they can have different local (area and shear) deformations. Correspondingly, in this level the skeleton-bilayer interactions are depicted as a slide in the lateral (i.e. in-plane) direction and a contact pressure in the normal direction. The viscous friction coefficient between the two layers is estimated by considering the skeleton density and the diffusivity of the transmembrane proteins within the lipid bilayer [34]. Numerically, quadrilateral finite elements (instead of triangular elements) are applied to avoid the shear-locking problem [35,36].

The properties of the inner layer (the protein skeleton) in the Level III model are obtained from a molecular-based model of the JC (Level II model). In this model we consider the JC as six Sps (each Sp is modeled as a nonlinear spring in the Level I model) surrounding an actin protofilament [32]. By using this model the mechanical properties of the skeleton at different deformations are computed and documented. In a typical information-passing algorithm, these properties are used by the level II model as constitutive laws of the inner layer.

The mechanical properties of Sp are obtained with a stress-strain model (Level I model) [2]. Sp is a biopolymer that can be overstretched (i.e. stretched beyond its contour length) due to unfolding of domains in it. Our model behaves similar to the conventional worm-like-chain (WLC) model in small to modest stretching. In large deformation a model based on the Arrhenius equation is applied to predict the occurrence and effect of domain unfolding (which is thermally activated). The predictions are summarized as constitutive laws of Sp and employed in the level II models.

The three-dimensional configuration and deformation predicted by the Level III model can be utilized by the Level II model to determine mesoscale mechanics and mechanical loads at the protein-to-protein and protein-to-lipid linkages so that the possibility of mechanically induced structural remodeling can be estimated.

3.2 Fluid-cell interaction

Owing to its small length scale, the flow field around a red blood cell is classified as the low-Reynolds number Stokes/Oseen flow. Mathematically, the problem can be linearized and formulated by using distributions of Stokeslets on the membrane surface. We apply a boundary-element method to solve the surrounding flow field and couple it with our multiscale model of the cell membrane. In this approach, the flow field is considered as the combined effect of an interfacial distribution of point forces called the single-layer Stokes flow potential, and an interfacial distribution of point sources with zero net strength accompanied by point-force dipoles known as the double-layer Stokes flow potential. This method solves the outside flow and the inside flow simultaneously [37]. Detailed mathematical formulations of this model is shown in the appendix.

In reality, the solid boundaries that form the slit are made of endothelial cells. These cells are covered by a layer of endothelial glycocalyx consisting of glycoproteins and other

h_b(nm)	μ_b(pN μm^{-1})	K_b(pN μm^{-1})	k_c(J)	ν_b(pN·s μm^{-1})
2.2	10^{-3}	9.6×10^{2}	2×10^{-19}	10^{-3}

Table 1 Parameters of the lipid bilayer. h_b: bilayer thickness (different from reality due to the homogeneous shell assumption), μ_b: bilayer shear stiffness (a very small value to stabilize numerical algorithm), K_b: bilayer areal stiffness, k_c: bilayer bending stiffness[41], ν_b: bilayer viscosity[42]

h_s(nm)	ν_s(pN s μm^{-1})	p_f(nm)	p_u(nm)	L_f(nm)
2	0.0125	11.12	0.8	6.39
L_u(nm)	$\Delta\Delta x^*$(nm)	$F_{1/2}$(pN)	μ_s (pN μm^{-1})	
39	12.6	12	5.7	

Table 2 Parameters of the cytoskeleton. h_s: cytoskeleton thickness, ν_s: cytoskeleton viscosity[44], p_f: persistence length of folded domains in Sp, p_u: persistence length of unfolded domains[2], L_f: contour length of folded domains[2], L_u: contour length of unfolded domains[2], $\Delta\Delta x^*$: the difference between the activation length of the unfolding process and that of the refolding process[2], $F_{1/2}$: the force corresponding to the state when half of the domains are unfolded[2], μ_s: initial shear modulus of the cytoskeleton[45]. A spectrin consists of 19 domains in our model.

molecules[38], which prevents the cell membrane from approaching too close to the boundaries. In our model this layer is depicted as a repulsive zone of thickness 0.1 μm on the boundaries. The thickness of our repulsive zone is close to the thickness of the exclusion zone used by Freund[26], although we use physical pressure to keep the cell away from the boundary, rather than artificially move it away when it comes too close. To elaborate, whenever the cell membrane penetrates this zone, it is pushed away along the normal direction of the boundary by a pressure whose magnitude increases linearly with the penetration distance. The exact magnitude of this pressure is chosen through numerical tests to guarantee that the penetration distance is much smaller than the thickness of the repulsive zone itself.

4 Results

We apply the aforementioned fluid-cell interaction algorithm to simulate the entire process of a RBC passing through a slit as defined in Fig. 1. The mean speed of the incoming flow ($\overline{U}$) is prescribed to be 100μm/s. According to *in vivo* experiments inside rat spleen[39], the transit time of RBC through a slit ranges from 0.02s to 60.5s, with the peak occurring around 0.1s (see Fig. 5 in that report). By using this incoming flow speed, the transit time predicted by our model falls into this range.

In the following simulations we consider the behavior of the system around three representative initial orientations: $\theta_0 = \phi_0 = 0^\circ$ (case 1), $\theta_0 = 0^\circ$ and $\phi_0 = 90^\circ$ (case 2), and $\theta_0 = 90^\circ$ and $\phi_0 = 0^\circ$ (case3). The physical properties of the lipid bilayer and the cytoskeleton are listed in Tables 1 and 2, respectively. Based on the reported diffusivity of transmembrane proteins[40], the friction coefficient per unit area c_f between the cytoskeleton and the lipid bilayer is estimated as $144\frac{\rho}{\rho_0}$ pN s μm^{-3} [34], where ρ and ρ_0 are the deformed and initial protein densities of the cytoskeleton, respectively. We note that the areal stiffness K_b of the lipid bilayer used in this study (9.6×10^2 pN μm^{-1}) is higher than the one used by Freund (67.7 pN μm^{-1})[26]. However, it is still significantly below the value used by Pozrikidis (10^5 pN μm^{-1})[43] or the one from measurements (5×10^5 pN μm^{-1})[41]. This is because high values of K_b require tiny time steps for numerical stability, which are computationally impractical. Subsequently, it is expected that our model will over-predict the magnitude of the area deformation. For that reason, the purpose of this modeling study is to explore the pattern of the area deformation on the membrane. We will also be able to predict the upper limit of the magnitude of the area expansion and compare that with the critical values that may lead to cell bursting. In our model the shear modulus of the cytoskeleton is a nonlinear function of deformation predicted by the level II model. Its initial value (the value without any deformation) is listed in Table 2 as μ_s.

In the finite-element implementation, both the lipid bilayer and the cytoskeleton are represented by 3000 elements (i.e. the total number of finite elements used is 6000). Correspondingly, 3000 boundary elements are employed on the cell membrane to resolve fluid effects. In addition, 1300 boundary elements are used on the solid boundaries, with the mesh density increased near the slit. The time step for simulation is chosen to be 4×10^{-6} second. To reduce computational effort, in the present study we concentrate on the case when the viscosity ratio $\Lambda = 1$ (see the appendix) so that the viscosities of the inner and outer fluids are the same (hereby chosen as 0.006 pN s μm^{-2} [46]).

To quantitatively measure the in-plane deformations of the bilayer and skeleton, we define two independent parameters, $\alpha = \lambda_1\lambda_2$ (representing the area deformation) and $\gamma = \lambda_1/\lambda_2$ (representing the shear deformation), where λ_1 and λ_2 are principle in-plane stretches (by definition $\lambda_1 > \lambda_2$). Due to the small time scale of the process, the sliding motion between the cytoskeleton and the lipid bilayer is negligible so that they have approximately the same deformations (as illustrated in our previous study[47], it takes O(10) seconds for significant sliding between the skeleton and the lipid bilayer to develop). For that reason, in the following results we do not distinguish between the in-plane deformation of the cytoskeleton and that of the lipid bilayer, despite the fact that there are tiny differences between them.

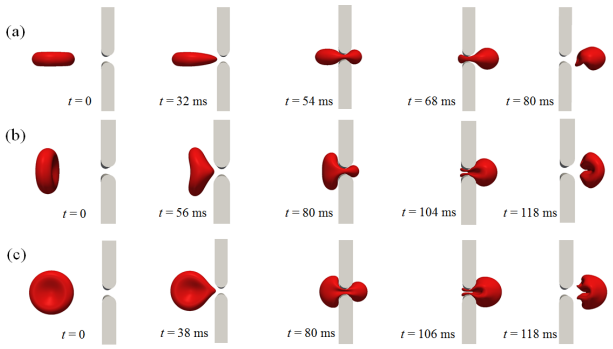

Fig. 2 Shape deformations of the cell as it passes through the slit with (a) case 1 ($\theta_0 = \phi_0 = 0°$), (b) case 2 ($\theta_0 = 0°$ and $\phi_0 = 90°$), and (c) case 3 ($\theta_0 = 90°$ and $\phi_0 = 0°$).

4.1 Deformation of the cell shape

The shape deformations of the cell when it passes through the slit with the three initial orientations are shown in Fig. 2. When $\theta_0 = \phi_0 = 0°$ the deformation is simple: during the passing process the part of the cell inside the slit is compressed while those outside are bloated to keep the total volume of the cell unaltered. The overall shape of the cell resembles a dumbbell with two bulges connected by a bridge (see Fig. 2a at 54 ms). Driven by the incoming flow, the membrane of the cell, together with the fluid inside, is transported from left to right until the left bulge completely disappears (at 68 ms). Afterwards the part of the cell in the slit is quickly retracted to catch up with the rest of the cell body in a process similar to the snapping of a cable when it breaks, during which the cell shape becomes unsymmetrical in the y direction.

A distinctively different behavior is observed when $\theta_0 = 0°$ and $\phi_0 = 90°$ (Fig. 2b). In a phenomenon described by Freund as 'infolding'[26], before leaving the slit the cell membrane folds inward to form a concave region (see Fig. 2b at $t = 104$ ms). The membrane that remains in the slit creates two 'tongues' with an empty space between them. Even after the cell leaves the slit (at $t = 118$ ms), the infolded shape is still preserved, leading to regions with high curvature on the cell membrane.

The occurrence of infolding is more pronounced in case 3 with $\theta_0 = 90°$ and $\phi_0 = 0°$ (Fig. 2c). It is seen that two concave regions appear even before the bulk of the cell enters the slit (at $t = 80$ ms). These two regions later combine to form a single infolded region (at $t = 106$ ms). Similar to the previous case, in the recovery phase the infolded region remains for a while.

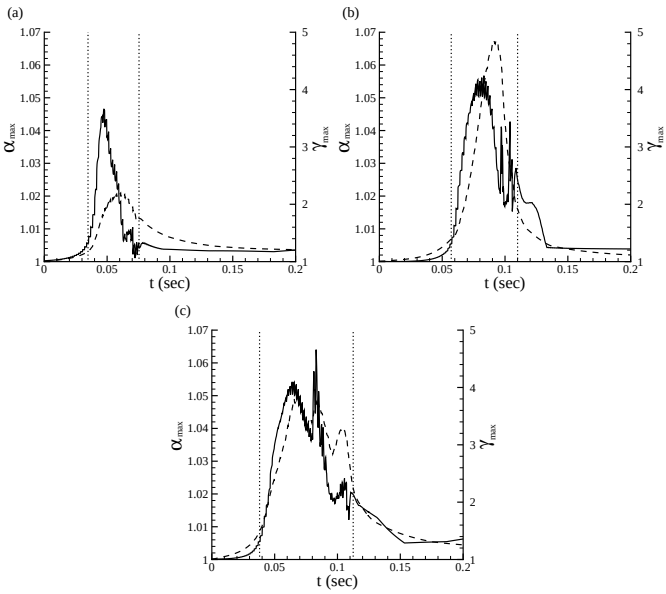

Fig. 3 Time histories of the maximum area (α_{max}, in solid lines) and shear (γ_{max}, in dashed lines) deformations of the membrane with (a) case 1 ($\theta_0 = \phi_0 = 0°$), (b) case 2 ($\theta_0 = 0°$ and $\phi_0 = 90°$), and (c) case 3 ($\theta_0 = 90°$ and $\phi_0 = 0°$). The dotted lines mark the start and end of the passing process.

4.2 Area and shear deformations of the membrane

In Fig. 3 we plot the time histories of the maximum values of the area formation α ($\alpha > 1$ corresponds to area expansion) and the shear deformation γ. In that figure we use dotted lines to mark the start and end of the passing process, defined as the moment the cell enters the slit and the moment it leaves, respectively. Not surprisingly, most of the area and the shear deformations occur when part of the cell is inside the slit. In all three cases, the maximum area expansion reaches 5-6%, slightly higher than the critical quasi-static areal strain (2-4%) that leads to membrane rupture[9,10], but significantly lower than the maximum value of areal strain a cell can sustain in dynamic conditions (40%). Considering the fact that the areal stiffness of the bilayer in our model is lower than the reported value, we conclude that pressure-induced cell bursting due to large area deformation of the bilayer is not likely with the given configurations and flow conditions.

Another phenomenon we notice in Fig. 3 is that the orientation of the cell greatly affects the transit time (i.e. the time it takes to pass through the slit). Indeed, in case 3 ($\theta_0 = 90°$ and $\phi_0 = 0°$) it takes twice as much time for the cell to pass through as case 1 ($\theta_0 = \phi_0 = 0°$). The longer the cell stays in the slit, the higher the chance for it to be captured and phagocytosed by macrophages. Although the transit time is not the focus of the current study, it is clear that more systematic simulations

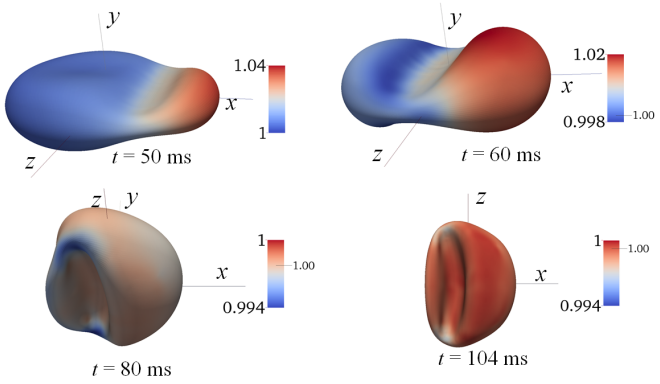

Fig. 4 Snapshots of the area deformation α with case 1.

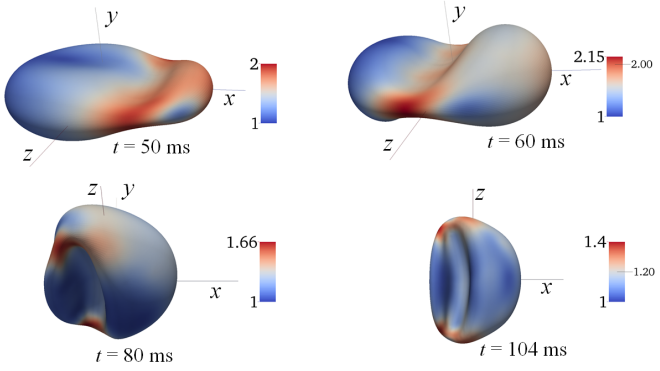

Fig. 5 Snapshots of the shear deformation γ with case 1.

are necessary in the future to document its dependence upon various parameters.

In Fig. 4 we display the distributions of area deformation at four different moments in case 1. It is seen that during the translocation area expansion occurs mostly on the right bulge that has already passed through the slit (see the snapshots at $t = 50$ ms and 60 ms). This suggests that as the internal fluid is pumped through the bridge the right bulge sustains large dynamic pressure. After the cell leaves the slit, the area deformation quickly disappears. For example, at $t = 104$ ms only localized (and very weak) area compression is left. Fig. 5 demonstrates the corresponding shear deformation at case 1. The shear deformation is concentrated near the bridge within the slit. Similar to the area deformation, after the translocation process the magnitude of shear deformation quickly drops. Simultaneously, the regions with significant shear deformation shrinks until it becomes highly localized (see the snapshot at $t = 104$ ms).

The distributions of area and shear deformations on the cell membrane with the other two initial orientations are plotted in

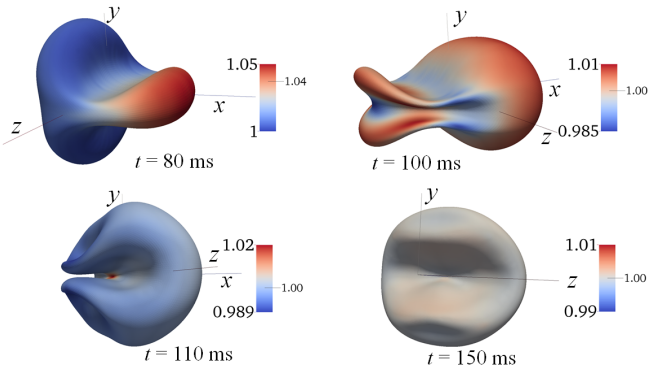

Fig. 6 Snapshots of the area deformation α with case 2.

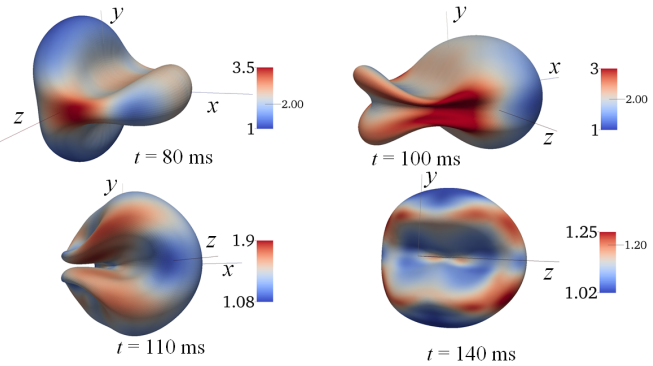

Fig. 7 Snapshots of the shear deformation γ with case 2.

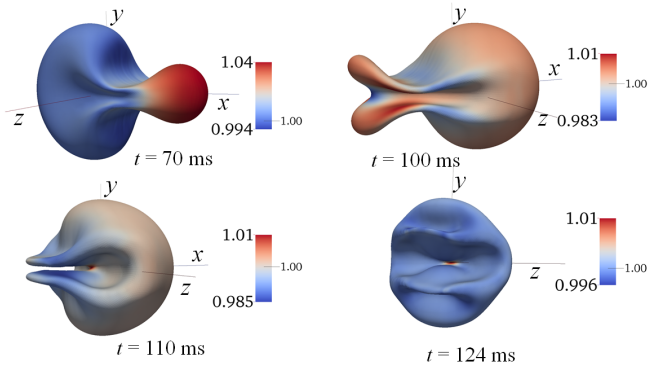

Fig. 8 Snapshots of the area deformation α with case 3.

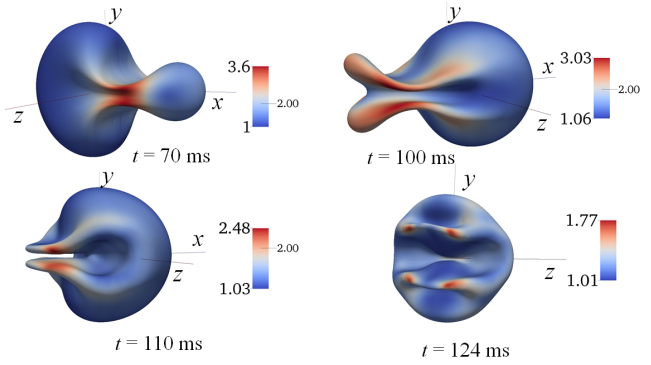

Fig. 9 Snapshots of the shear deformation γ with case 3.

Figs. 6 to 9. In all of these cases the maximum area deformation occurs in the right bulge when the cell is in a dumbbell shape. Meanwhile the maximum shear deformation occurs on the bridge, where the cell sustains stretching load. After completely leaving the slot, we again see that these in-plane deformations plummet in magnitude.

It is seen that in all three cases during the recovery phase (after the cell has completely left the slit) the membrane deformation undergoes two trends: the decrease in the magnitude of deformation and the shrink of the affected region. Due to the second trend the membrane deformation quickly becomes localized. This is most pronounced in case 3, where shear deformation concentrates around four spots at the edge of the tongues (see Fig. 9 at $t = 124$ ms). These spots, as shown in the figure, are also places with high out-of-the-plane (i.e. bending) deformation. Such deformation concentration, as we shall show later, coincides with large negative (dissociation) pressure between the cytoskeleton and the lipid bilayer.

4.3 Contact pressure between the cytoskeleton and the bilayer

The contact pressure between the cytoskeleton and the lipid bilayer is an important parameter associated with mechanically induced structural remodeling of the system. As mentioned in the introduction, the connectivity between the skeleton and the bilayer is achieved *via* transmembrane proteins (band 3 and glycophorin C) embedded in the bilayer, which are then linked to the skeleton through other proteins (e.g. ankyrin, protein 4.1 and protein 4.2). Sufficiently large mechanical loads may rupture the linkages between these proteins as well as the protein-to-lipid linkage, leading to skeleton-bilayer dissociation. These mechanical loads are closely associated with the contact pressure p_c, defined as the contact force per unit area between the two layers in our level 3 model. Positive values of p_c refers to the scenario when the two layers are pushed towards each other, whereas negative values correspond to the dissociation trend between the two (which is what we are interested in).

Fig. 10 shows the time histories of the maximum dissociation pressure between the skeleton and lipid bilayer (again we use two dotted vertical lines to mark the start and end of the translocation). A noteworthy phenomenon is that large values of p_c may actually occur during the recovery phase after the translocation. Indeed, in case 3 (in which the cell deformation is more significant than the other two cases) the peak value of p_c almost reaches -1000 pN/μm^2 (herein the minus sign refers to the dissociation tendency). To put this in context, our previous simulations[33] show that in a typical micropipette aspiration (by applying a negative pressure of 256 pN/μm^2 in a cylindrical pipette with radius $R_p = 0.668$ μm) of a cell with similar properties, the peak value of dissociation pressure is only -130 pN/μm^2.

The dissociation pressure between the cytoskeleton and the lipid bilayer after the passing progress may be attributed to the differences in the shape recovery progress of these two components. In our model the biconcave shape coincides with the lowest strain energy configuration of the lipid bilayer so that it will automatically re-establish this shape after the cell leaves the slit. The cytoskeleton, on the other hand, is simply carried by the lipid bilayer towards the biconcave configuration. This induces interaction pressure between the two. Although the bending stiffness of the cytoskeleton is negligible compared with that of the lipid blayer, when there is in-plane deformation in it the tension may impart resistance to out-of-the-plane (bending) deformations. This is likely an explanation of the fact that large values of contact pressure coincide with large in-plane deformations.

To further investigate the occurrence of large dissociation pressure during the recovery phase, in Fig. 11 we plot the distribution of contact pressure in these three cases in the recov-

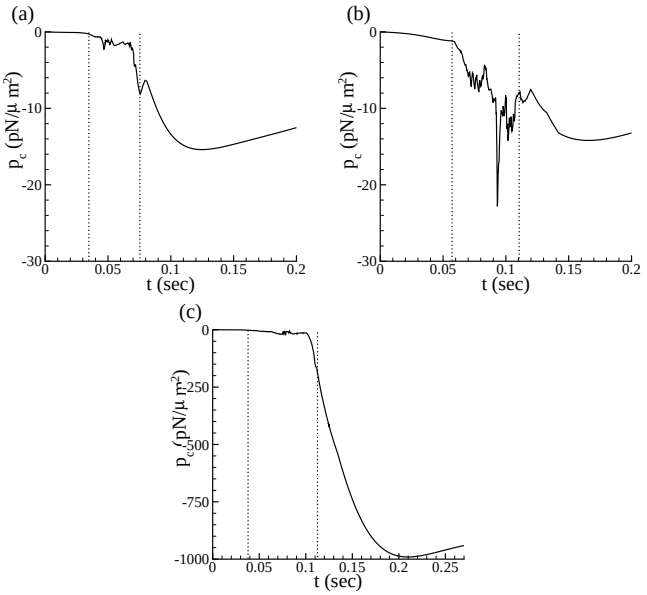

Fig. 10 Time histories of the contact pressure of the membrane with (a) case 1, (b) case 2, and (c) case 3. The dotted lines mark the start and end of the passing process.

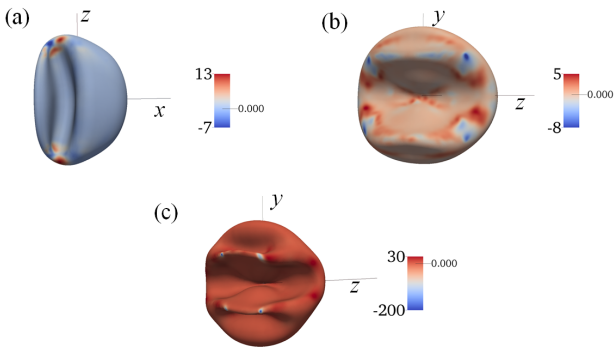

Fig. 11 Snapshots of the distribution of contact pressure (the unit of the scale is pN/μm^2) in the recovery phase. (a) case 1 (at $t = 104$ ms), (b) case 2 (at $t = 140$ ms), and (c) case 3 (at $t = 124$ ms).

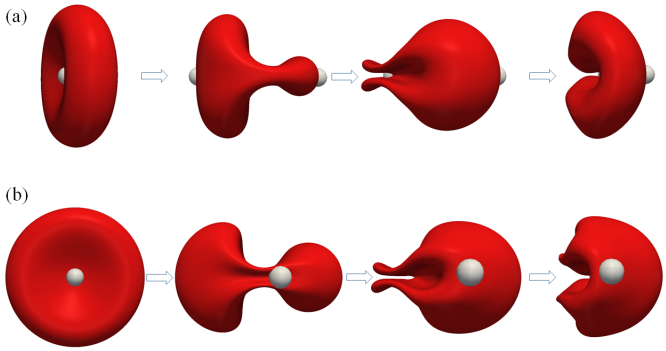

Fig. 12 Locations of the dimple elements (marked by the spheres) during the translocation for (a) case 2 and (b) case 3.

ery phase (at $t = 104$ ms, 140 ms, and 124 ms, respectively). It is seen that similar to the in-plane deformations at these moments, the contact pressure is also localized (especially in the third case). In the first case negative (dissociation) pressure occurs around two locations (close to the locations with concentrated area and shear deformations shown in Figs. 4 and 5). In the second and third cases it appears at four locations, two on the upper tongue and the other two on the lower one, again coinciding with distributions of area and shear deformations shown in Figs. 6 to 9.

Although they both involve infolding deformation, the key difference between case 2 and case 3 lies in the locations of the dimple elements (i.e. the membrane elements originally located at the dimple areas in the natural configuration) during the translocation. As shown in Fig. 12, in case 2 the dimple elements remain on the central axis (the x axis), whereas in case 3 they remain in two sides away from the x axis. Due to the shape memory effect[48] these elements will always try to return to their original locations (the dimples) after the translocation. With this requirement it is seen from the figure that in case 2 it is much easier for the cell to recover its biconcave shape compared with case 3 (in which the infolded region will eventually form the rim of the biconcave shape). This provides an explanation for the large differences between these two cases in terms of the recovery process and the contact pressure.

5 Conclusions and discussion

By using a multiscale fluid-cell interaction model, we numerically investigated dynamics of a red blood cell being pushed through a slit by an incoming flow. Rather than documenting the behavior under different conditions (e.g. incoming flow speed, viscosity ratio between the internal and outside fluids, and lateral offset between the initial location of the cell and the slit; for computational reason, parametric studies will be conducted in the future), we focus on a phenomenologi-

cal investigation about the temporal and spacial distributions of the deformations of the membrane as well as the contact pressure between its two components, the lipid bilayer and the cytoskeleton.

Depending on the initial orientation of the cell, during the translocation procedure two different behaviors in the shape deformation of the cell have been recorded. In the first scenario the cell forms a dumbbell shape when it squeezes through the slit. The second scenario is characterized by the occurrence of infolding, in which two tongues are formed with a concave region between them. These two cases are similar in terms of the maximum area deformation, whereas infolding may induce large shear deformation. Inflated by the internal fluid that is pumped through the slit, the maximum area expansion occurs on the right bulge formed by the membrane that has already passed through. Meanwhile, the maximum shear deformation occurs on the bridge (the part that is still within the slit), which is stretched in the process. On the other hand, large dissociation pressure appears after the cell itself has completely passed through the slit and tries to re-establish its original configuration. Without infolding, it concentrates on two spots. When infolding occurs, four spots with large dissociation pressure are observed. In a case with infolding ($\theta = 90^\circ$ and $\phi_0 = 0^\circ$) following the localization of membrane deformation the peak value of the dissociation pressure surpasses that in a typical micropipette aspiration. However, further tests show that in this case infolding (and the subsequent large negative pressure) is only achieved within a tiny range of parameters (when $\phi_0 = 0^\circ$ the value of θ has to be between 87° and 93°). In contrast, with $\theta = 0^\circ$ infolding occurs when $70^\circ < \phi_0 < 110^\circ$. This case, on the other hand, is associated with less membrane deformation and much smaller contact pressure between the two layers. This may provide an explanation why a normal RBC can go through the spleen many times during its lifetime without losing its structural stability and integrity.

The occurrence of large dissociation pressure (which may lead to skeleton-lipid dissociation and vesiculation) suggests the possibility of mechanically induced structure remodeling. Large negative pressure may lead to mechanically induced skeleton-bilayer dissociation and vesiculation. By using the critical mechanical loads associated with the rupture of intra-protein, inter-protein and protein-to-lipid linkages (some of these are available from literature), it is possible to numerically predict the occurrence of these structural remodelings. Our problem is transient so that dynamic (rather than quasi-static) mechanisms have to be considered. In addition, the negative contact pressure is localized. It is not known if the local dissociation it creates can trigger a domino effect which eventually leads to vesiculation.

One important factor that has not been considered in this study is the stress-free (or reference) state of the cytoskeleton. It refers to the configuration of the membrane with zero stress inside the cytoskeleton. In the current study the reference state coincides with the natural biconcave state of the cell. However, recently there are experimental and numerical evidences suggesting that this may not be accurate[49–52]. Instead, a spheroidal reference state can explain the natural shape[53,54], the shape memory effect[48], and the dynamics of RBCs in low shear rate flows[49]. Such a reference state leads to a distribution of prestress inside the cytoskeleton when it is in the natural biconcave state. Since the magnitude of this prestress is small, its effect on the cell dynamics during large deformations (e.g. when the cell is still in the slit) is expected to be insignificant. On the other hand, it may affect the recovery procedure of the cell as the in-plane deformation of the skeleton decreases. Since the reference state plays a pivotal role in the shape recovery of the bilayer and the skeleton, its effect on the contact pressure between them may be profound. Future studies in this direction are thus necessary.

Finally, it will be interesting to investigate the effects of changes in the mechanical or morphological conditions (e.g. shear stiffness, volume-to-surface area ratio) of RBC on its mechanical performance in the spleen. These changes can be caused by mutations, diseases, or storage. We are particularly interested in how the changes in the structural stability and robustness of the cell affect its survivability in this environment. The destruction of RBC in large quantity in the spleen leads to anemia. The correlation between these changes and the transit time through a slit is another important topic. Abnormal cells may either be blocked or spend longer time in the spleen, increasing their chance of being destroyed by macrophages.

Appendix

The boundary-element method is based on the boundary-integral equation of interface dynamics for Stokes flow[37,55], according to which at any point $\mathbf{x}_0$ on the cell surface the velocity $\mathbf{v}$ satisfies

$$\begin{aligned}\mathbf{v}(\mathbf{x}_0) &= \frac{2}{1+\Lambda}\bar{\mathbf{v}}(\mathbf{x}_0) \\ &- \frac{1}{4\pi\eta_1(\Lambda+1)}\iint_{\Gamma_c+\Gamma_b}\mathbf{G}(\mathbf{x},\mathbf{x}_0)\cdot\Delta\mathbf{t}(\mathbf{x})d\Gamma(\mathbf{x}) \\ &+ \frac{1-\Lambda}{4\pi(1+\Lambda)}\text{⨍⨍}_{\Gamma_c}\mathbf{v}(\mathbf{x})\cdot\mathbf{T}(\mathbf{x},\mathbf{x}_0)\cdot\mathbf{n}(\mathbf{x})d\Gamma(\mathbf{x}), \quad (1)\end{aligned}$$

where Γ_c is the fluid-cell boundary and Γ_b is the surface of the solid boundaries. $\bar{\mathbf{v}}$ is the undisturbed flow velocity. η_1 is the viscosity of the external fluid, η_2 is the viscosity of the internal fluid, and $\Lambda = \eta_2/\eta_1$. $\Delta\mathbf{t}$ is the difference between the traction in the outside surface of the cell membrane and the traction in the inside surface of the membrane. $⨍⨍$ denotes the principal value integration. The matrix $\mathbf{G}$ contains the triply

periodic Green's function for velocity G_{ij}, and the matrix $\mathbf{T}$ contains the triply periodic Green's function for stress T_{ijk}[56]. Physically, the second term in the right hand side of Eq. (1) represents contribution from the distribution of point forces and the third term represents contributions from point sources and point force dipoles.

For any point $\mathbf{x}_0$ on the solid boundaries Γ_b, the no-slip/no-flux boundary condition is

$$\begin{aligned} 0 &= \frac{2}{1+\Lambda}\overline{\mathbf{v}}(\mathbf{x}_0) - \frac{1}{8\pi\eta_1}\iint_{\Gamma_c+\Gamma_b}\mathbf{G}(\mathbf{x},\mathbf{x}_0)\cdot\Delta\mathbf{t}(\mathbf{x})d\Gamma(\mathbf{x}) \\ &+ \frac{1-\Lambda}{8\pi}\iint_{\Gamma_c}\mathbf{v}(\mathbf{x})\cdot\mathbf{T}(\mathbf{x},\mathbf{x}_0)\cdot\mathbf{n}(\mathbf{x})d\Gamma(\mathbf{x}). \end{aligned} \quad (2)$$

In the boundary-element formulation, we discretize both the cell surface and the solid boundaries into quadruple elements (incidently, the boundary elements on the cell surface coincide with the finite elements on the lipid bilayer). With N_c collocation points on the cell surface and N_b points on the solid surfaces, Eq. (1) is written in its discretized form as

$$\mathsf{v} = \overline{\mathsf{v}}_c - \mathsf{S}_{cb}\mathsf{q}_b - \mathsf{S}_{cc}\mathsf{q}_c + \mathsf{D}_{cc}\mathsf{v}. \quad (3)$$

Meanwhile, the boundary condition (Eq. (2)) becomes

$$0 = \overline{\mathsf{v}}_b - \mathsf{S}_{bb}\mathsf{q}_b - \mathsf{S}_{bc}\mathsf{q}_c + \mathsf{D}_{bc}\mathsf{v}, \quad (4)$$

where the global velocity vector v (with $3N_c$ components) includes velocities at all collocation points on Γ_c. The vector $\overline{\mathsf{v}}_c$ contains the undisturbed velocities at these points (including the factor $2/(1+\Lambda)$), and the vector $\overline{\mathsf{v}}_b$ consists of the undisturbed velocities at the collocation points on Γ_b. The matrix S_{cb} ($3N_c \times 3N_b$) and the matrix S_{cc} ($3N_c \times 3N_c$) are influence matrices representing the second term on the righthand side of Eq. (1). The matrix D_{cc} ($3N_c \times 3N_c$) comes from the third term on the righthand side of Eq. (1). The other influence matrices (S_{bb}, S_{bc}, and D_{bc}) are from Eq. (2).

In general cases Eqns. (3) and (4) are coupled. The most effective way to solve them simultaneously is through an iterative algorithm, which is extremely expensive (considering the fact that large number of elements are necessary on the cell surface to resolve its complicated deformations). However, we note that in the case when $\Lambda = 1$, Eqns. (3) and (4) are simplified as

$$\mathsf{v} = \overline{\mathsf{v}}_c - \mathsf{S}_{cb}\mathsf{q}_b - \mathsf{S}_{cc}\mathsf{q}_c, \quad (5)$$

and

$$0 = \overline{\mathsf{v}}_b - \mathsf{S}_{bb}\mathsf{q}_b - \mathsf{S}_{bc}\mathsf{q}_c. \quad (6)$$

In this special case evaluation of the double-layer integrations is avoided. More importantly, the two equations are now decoupled so that they can be solved much more efficiently. Specifically, from Eq. (6) we evaluate q_b as $\mathsf{S}_{bb}^{-1}\left[\overline{\mathsf{v}}_b - \mathsf{S}_{bc}\mathsf{q}_c\right]$, where q_c is obtained in the structural part of the model. It is then substituted into Eq. (5) to find v.

References

1 M. Rief, J. Pascual, M. Saraste and H. Gaub, *J. Mol. Biol.*, 1999, **286**, 553–561.
2 Q. Zhu and R. Asaro, *Biophys. J.*, 2008, **94**, 2529–2545.
3 T. DeSilva, K.-C. Peng, K. Speicher and D. Speicher, *Biochem.*, 1992, **31**, 10872–10878.
4 X. An, M. Lacomte, J. Chasis, N. Mohandas and W. Gratzer, *J. Biol. Chem.*, 2002, **277**, 31796–31800.
5 W. Anong, T. Weis and P. Low, *J. Biol. Chem.*, 2006, **281**, 22360–22366.
6 X. An, Y. Takakuwa, W. Nunomura, S. Manno and N. Mohandas, *J. Biol. Chem.*, 1996, **271**, 33187–33191.
7 J. Butler, N. Mohandas and R. Waugh, *Biophy. J.*, 2008, **95**, 1826–1836.
8 J. Li, G. Lykotrafitis, M. Dao and S. Suresh, *Proc. Natl. Acad. Sci. U.S.A.*, 2007, **104**, 4937–4942.
9 E. Evans, R. Waugh and L. Melnik, *Biophys. J.*, 1976, **16**, 585–595.
10 B. Daily, E. Elson and G. Zahalak, *Biophy. J.*, 1984, **45**, 671–682.
11 F. Li, C. Chan and C. Ohl, *Biophy. J.*, 2013, **105**, 872–879.
12 S. Deutsch, J. Tarbell, K. Manning, G. Rosenberg and A. Fontaine, *Annu. Rev. Fluid Mech.*, 2006, **38**, 65–86.
13 T. Fischer, M. Stohr-Liesen and H. Schmid-Schonbein, *Science*, 1978, **202**, 894–896.
14 D. Barthès-Biesel, *J. Fluid Mech.*, 1980, **100**, 831–853.
15 S. Keller and R. Skalak, *J. Fluid Mech.*, 1982, **120**, 27–47.
16 C. Eggleton and A. Popel, *Phys. Fluids*, 1998, **10**, 1834–1845.
17 M. Abkarian, M. Faivre and A. Viallat, *Phys. Rev. Lett.*, 2007, **98**, 188302.
18 H. Noguchi, *Phys. Rev. E*, 2009, **80**, 021902.
19 P. Vlahovska, Y. Young, G. Danker and C. Misbah, *J. Fluid Mech.*, 2011, **678**, 221–247.
20 A. Yazdani, R. Kalluri and P. Bagchi, *Phys. Rev. E*, 2011, **83**, 046305.
21 T. Fischer and R. Korzeniewski, *J. Fluid Mech.*, 2013, **736**, 351–365.
22 C. Pozrikidis, *Phys. Fluids*, 2005, **17**, 031503.
23 C. Pozrikidis, *Annu. Biomed. Engr.*, 2005, **33**, 165–178.
24 D. Fedosov, M. Peltomaki and G. Gompper, *Soft Matter*, 2014, **10**, 4258–4267.
25 D. A. Fedosov, B. Caswell and G. E. Karniadakis, *Biophys. J.*, 2011, **100**, 2084–2093.
26 J. Freund, *Phys. Fluids*, 2013, **25**, 110807.
27 D. Halpern and T. Secomb, *J. Fluid Mech.*, 1992, **244**, 307–322.
28 G. Gompper and D. Kroll, *Phys. Rev. E*, 1995, **52**, 4198—4208.
29 H. Noguchi and G. Gompper, *PNAS*, 2005, **40**, 14159—14164.
30 D. Quinn, I. Pivkin, S. Wong, K. Chiam, M. Dao, G. Karniadakis and S. Suresh, *Ann. Biomed. Engr.*, 2011, **39**, 1041—1050.
31 G. Delplaine *et al.*, *Blood*, 2011, **117**, e88–e95.
32 Q. Zhu, C. Vera, R. Asaro, P. Sche and L. A. Sung, *Biophys. J.*, 2007, **93**, 386–400.
33 Z. Peng, R. Asaro and Q. Zhu, *Phys. Rev. E*, 2010, **81**, 031904.
34 Z. Peng, R. Asaro and Q. Zhu, *J. Fluid Mech.*, 2011, **686**, 299–337.
35 T. Belytschko, W. Liu and B. Moran, *Nonlinear Finite Elements for Continua and Structures*, John Wiley, New York, 2000.
36 J. Walter, A. Salsac, D. Barthès-Biesel and P. L. Tallec, *Int. J. Num. Methods Engr.*, 2010, **83**, 829–850.
37 C. Pozrikidis, *Boundary Integral and Singularity Methods for Linearized Viscous Flow*, Cambridge University Press, 1992.
38 S. Weinbaum, J. Tarbell and E. Damiano, *Annu. Rev. Biomed. Eng.*, 2007, **9**, 121–167.
39 I. MacDonald, D. Ragan, E. Schmidt and A. Groom, *Microvascular Res.*, 1987, **33**, 118—134.
40 G. Kodippili, J. Spector, C. Sullivan, F. Kuupers, R. Labotka, P. Gallagher, K. Ritchie and P. Low, *Blood*, 2009, **113**, 6237—6245.
41 N. Mohandas and E. A. Evans, *Annu. Rev. Biophys. Biomol. Struct.*, 1994,

23, 787–818.
42 W. K. Otter and S. A. Shkulipa, *Biophys. J.*, 2007, **93**, 423–433.
43 C. Pozrikidis, *Phys. Fluids*, 2005, **17**, 031503.
44 R. Tran-Son-Tay, S. Sutera and P. Rao, *Biophys. J.*, 1984, **46**, 65–72.
45 E. Evans and P. Skalak, *Mechanics and Thermodynamics of Biomembranes*, CRC Press, Boca Raton, FL, 1980.
46 S. Chien, *Annu. Rev. Ohysiol.*, 1987, **49**, 177—192.
47 Z. Peng and Q. Zhu, *Soft Matter*, 2013, **9**, 7617–7627.
48 T. Fischer, *Biophys. J.*, 2004, **86**, 3304–3313.
49 J. Dupire, M. Socol and A. Viallat, *Proc. Natl. Acad. Sci. U.S.A.*, 2012, **109**, 20808–20813.
50 K. Tsubota, S. Wada and H. Liu, *Biomech. Model Mechanobiol.*, 2014, **13**, 735–746.
51 Z. Peng, A. Mashayekh and Q. Zhu, *J. Fluid Mech.*, 2014, **742**, 96–118.
52 D. Cordasco, A. Yazdani and P. Bagchi, *Phys. Fluids*, 2014, **26**, 041902.
53 G. Lim, M. Wortis and R. Mukhopadhyay, *Proc. Natl. Acad. Sci. U.S.A.*, 2002, **99**, 16766–16769.
54 G. Lim, M. Wortis and R. Mukhopadhyay, in *Soft Matter, Vol 4: Lipid Bilayers and Red Blood Cells*, ed. G. Gompper and M. Schick, Wiley-VCH, Weinheim, Germany, 2008.
55 H. Zhao, A. Isfahania, L. Olsonc and J. Freund, *J. Comput. Phys.*, 2010, **229**, 3726.
56 C. Pozrikidis, *J. Engr. Math.*, 1995, **30**, 79–96.